

PAPER • OPEN ACCESS

Multi-objective optimization of three-dimensional riblet surfaces for hydrodynamic and acoustic performance

To cite this article: Zixiao Wei *et al* 2025 *Bioinspir. Biomim.* **20** 066002

View the [article online](#) for updates and enhancements.

You may also like

- [Hydrodynamic properties of biomimetic shark skin: effect of denticle size and swimming speed](#)
August G Domel, Gino Domel, James C Weaver *et al.*
- [Hydrodynamic function of biomimetic shark skin: effect of denticle pattern and spacing](#)
Li Wen, James C Weaver, Patrick J M Thornycroft *et al.*
- [Characterization of shark skin properties and biomimetic replication](#)
Stan R R Baeten, Ana Kochovski, Jovana Jovanova *et al.*

Bioinspiration & Biomimetics



PAPER

OPEN ACCESS

RECEIVED
16 February 2025

REVISED
2 July 2025

ACCEPTED FOR PUBLICATION
2 September 2025



PUBLISHED
6 October 2025

Original content from this work may be used under the terms of the [Creative Commons Attribution 4.0 licence](#).

Any further distribution of this work must maintain attribution to the author(s) and the title of the work, journal citation and DOI.



Multi-objective optimization of three-dimensional riblet surfaces for hydrodynamic and acoustic performance

Zixiao Wei^{1,3}, Zilan Zhang^{1,3}, Dahyun Daniel Lim¹, Justin Rey² , Matthew Jones²  and Grace X Gu^{1,*} 

¹ Department of Mechanical Engineering, University of California, Berkeley, CA 94720, United States of America

² MIT Lincoln Laboratory, Lexington, MA 02421, United States of America

³ These authors contributed equally.

* Author to whom any correspondence should be addressed.

E-mail: ggu@berkeley.edu

Keywords: flow-induced noise, underwater acoustics, Bayesian optimization, computational fluid dynamics, bioinspired riblet design

Supplementary material for this article is available [online](#)

Abstract

Riblets inspired by the dermal denticles of shark skin are widely recognized for their drag-reducing performance. Although previous research has predominantly focused on two-dimensional riblet geometries, three-dimensional (3D) topographies remain underexplored due to the complex architecture of denticle-inspired surfaces. Natural riblet arrays, comprising thousands of interconnected dermal denticles, pose challenges in terms of parameterization, simulation, and fabrication. This work addresses these challenges by introducing a 3D, riblet-reinforced surface topography design that reduces drag, suppresses flow-induced noise, and simplifies both parameterization and prototyping, ultimately providing a scalable solution for towed array sonar applications. Leveraging Bayesian optimization, our computational fluid dynamics (CFD) results reveal that the optimal design decreases the overall sound pressure level by 6.87 dB and reduces drag by 0.34%, effectively balancing noise mitigation with hydrodynamic performance. The design that achieves the greatest noise reduction lowers flow noise by 8.81 dB, albeit with a slight increase in drag. The most effective design for drag reduction yields a 5.18% decrease, accompanied by significant noise suppression across key frequency bands. Flow field analysis demonstrates that our design alters the near-wall vorticity dynamics by promoting the formation of vortex rings that detach from the surface, thereby reducing turbulent energy transfer and limiting sound pressure fluctuations relative to a smooth surface design. To this end, the combination of CFD simulations and Bayesian optimization offers an efficient pathway to refine riblets-reinforced surface topographies, paving the way for advanced bioinspired designs that improve acoustic performance and efficiency in underwater applications.

1. Introduction

Bio-inspired designs, drawing inspiration from the unique structures and mechanisms found in nature, have shown great potential for advancing engineering applications across various domains [1–10]. Such unique structure and surface characteristics have evolved to provide animals with superior adaptability and functionality in their respective environments. A significant focus of bio-inspired design research has been on studying and replicating those surface patterns and topologies of marine animals

such as sharks and dolphins due to their remarkable hydrodynamic advantages [11–14]. One example of such bio-inspired innovation is the implementation of riblet topologies, which mimic the denticle structures found on the shark skin. There have been research illustrating the exceptional promise of riblets in reducing the hydrodynamic drag [11, 14–17]. Frohnapfel *et al* [15] carried out experimental investigations to validate the impact of surface-embedded grooves on turbulent drag reduction. Ott *et al* [14] have looked into designing shark skin denticle structure with five parameters. By adjusting the size, shape,

and orientation of the denticles, they demonstrated how modifications to the boundary layer dynamics can effectively reduce drag. Dean and Bhushan [11] defined a metric for selecting the optimal riblet dimensions in reducing the flow drag. Riblet designs ensure that vortices remain above the grooves, allowing the high-velocity vortices to interact only with the riblet crests, where most shear stresses are localized.

On the other hand, recent studies on riblet surfaces have further demonstrated their effectiveness in mitigating flow-induced noise [18]. One of the key applications of riblet technology is in towed array sonar (TAS), which are widely used for underwater signal detection [19–21]. During operation, the interaction between the TAS and the surrounding fluid generates flow noise, interfering with the detection of target signals. This flow-induced noise originates from pressure fluctuations generated by the interaction between the turbulent boundary layer (TBL) and the array's surface [22–25]. Earlier research on TAS focused on improving the signal-to-noise ratio (SNR) by separating target signals from noise [21]. Recent advancements have shifted attention toward directly reducing the noise generated by such interactions using riblet designs. Similar to their drag-reducing mechanism, riblets alter surface flow patterns to minimize noise. Wei *et al* [18] computationally investigated various bio-inspired riblet topologies applied to TAS surfaces. The study revealed significant reductions in both noise and drag, particularly with rectangular riblets. A preliminary parametric analysis further indicated that finer and more closely spaced riblet geometries could enhance both acoustic and hydrodynamic performance.

Optimizing riblet geometry hence holds great promise for reducing both drag and noise. This potential has been explored through computational fluid dynamic (CFD) simulations, which provides detailed insights into complex flow interactions and facilitates parametric design and optimization [14, 26–28]. Previous studies on riblets have focused primarily on drag reduction, often limiting their scope to two-dimensional (2D) designs with no geometric variation along the streamwise direction. The investigation of high-fidelity, three-dimensional (3D) topographies that emulate the features of biological systems such as dermal denticles remains limited [29–31]. Natural riblet surfaces, as exemplified by shark skin, consist of thousands of interconnected denticle units that collectively influence flow dynamics. Sharks excel in underwater environments by utilizing these specialized surfaces to adapt effectively across a variety of flow conditions. By capturing the 3D architecture of such biological systems, it is possible to achieve more pronounced effects in flow

noise and drag reduction under diverse scenarios compared to 2D riblets.

This study investigates a 3D riblet design that better emulate natural systems by incorporating streamwise geometric variations, drawing inspiration from shark skin denticles to develop and parameterize a novel surface topography. The denticles are generated on a scaled TAS model for high-fidelity simulations. The primary goal is to assess sound reduction across different frequency ranges alongside towing drag performance, aiming to enhance both SNR and hydrodynamic efficiency. To achieve this, we created a CFD model to simulate the performance of a riblets-reinforced array surface (RRAS) characterized by embedded 3D topographies, as demonstrated in figure 1(a). Utilizing this parameterized design template, we employ a Bayesian multi-objective optimization framework to efficiently navigate the high-dimensional design space. This approach enables a balanced evaluation of competing objectives, flow noise and drag, by guiding the search toward Pareto-optimal solutions that offer tradeoffs unattainable through single-objective methods. Key geometric parameters, including riblet height, spacing, and ridge ratios, are systematically varied to assess their effects. To communicate the methodology and findings, the remainder of this paper is structured as follows: section 2 details the design parameterization, CFD methodology, and optimization strategy; section 3 explains the rationale for the selected performance metrics and presents the corresponding simulation results; and section 4 highlights critical trends and flow structures revealed by the optimized geometries, demonstrating the effectiveness of multi-objective optimization in addressing coupled aerodynamic and acoustic performance goals.

2. Method

Here the general riblet dimensions and corresponding CFD setup are described. These are derived from our previous research on 2D riblets [18], modified to adapt the exploration of the 3D case. The riblet's wavelength s and amplitude h are determined by the following equations:

$$h = \sqrt{\frac{2}{C_f}} \left(\frac{h^+ \nu}{U_\tau} \right) \quad (1)$$

$$s = \sqrt{\frac{2}{C_f}} \left(\frac{s^+ \nu}{U_\tau} \right) \quad (2)$$

where C_f is the skin friction coefficient, U_τ is the shear velocity, ν is the kinematic viscosity, and h^+ , s^+ are the dimensionless wave amplitude and length. According to Lee and Lee [32], $h^+ = 12.6$ and $s^+ = 25.2$ provide a suitable fit for underwater applications. Therefore, these values are adopted as

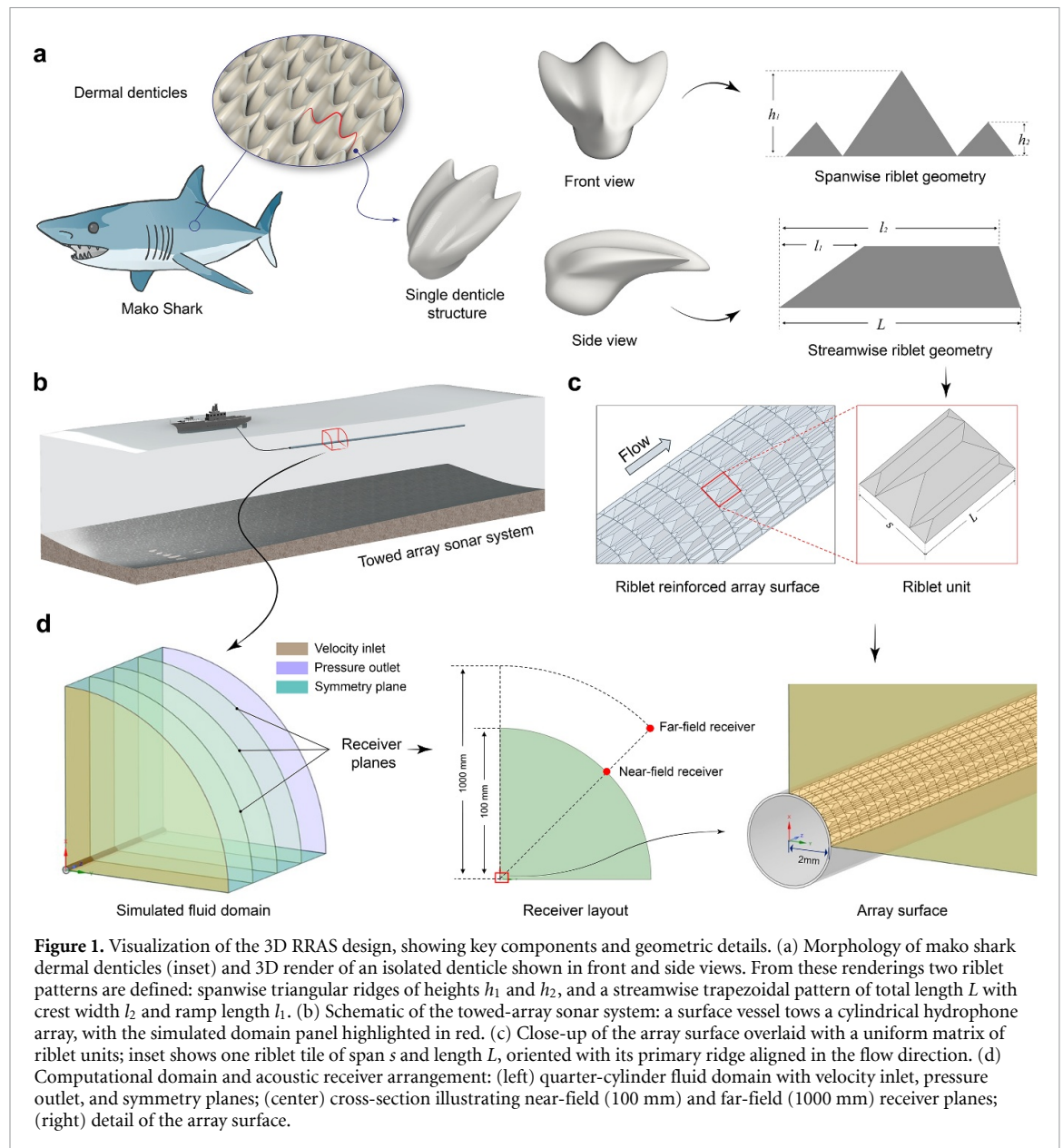


Figure 1. Visualization of the 3D RRAS design, showing key components and geometric details. (a) Morphology of mako shark dermal denticles (inset) and 3D render of an isolated denticle shown in front and side views. From these renderings two riblet patterns are defined: spanwise triangular ridges of heights h_1 and h_2 , and a streamwise trapezoidal pattern of total length L with crest width l_2 and ramp length l_1 . (b) Schematic of the towed-array sonar system: a surface vessel tows a cylindrical hydrophone array, with the simulated domain panel highlighted in red. (c) Close-up of the array surface overlaid with a uniform matrix of riblet units; inset shows one riblet tile of span s and length L , oriented with its primary ridge aligned in the flow direction. (d) Computational domain and acoustic receiver arrangement: (left) quarter-cylinder fluid domain with velocity inlet, pressure outlet, and symmetry planes; (center) cross-section illustrating near-field (100 mm) and far-field (1000 mm) receiver planes; (right) detail of the array surface.

the initial guess in the Bayesian optimization process for this study.

2.1. RRAS design and parametrization

Figures 1(b) and (c) illustrates the TAS system used in this study and the 3D RRAS design. The streamwise modifications segment the longitudinal riblet ridges into smaller units, introducing unique surface features. These topographical changes are achieved through extruded cuts applied along both the streamwise and spanwise directions (see figure 1(a)). The proposed design incorporates ridges with two distinct amplitudes, h_1 and h_2 , emulating the structure of sharkskin denticles, characterized by a primary ridge flanked by two smaller side ridges [33]. Arranged along a quarter-circle surface, the spanwise riblet pattern spans five sets of ridges, each maintaining a total base length of $s = 0.6\text{mm}$. In terms of the

streamwise cross-section, the 3D riblet denticle unit exhibits a trapezoidal geometry with a total length L . The lengths of the front and rear sides at the top of the trapezoid are denoted as l_1 and l_2 , respectively. The height of the trapezoid varies between the primary and side ridges, contributing to the differentiated structure of the riblet denticles.

Table 1 summarizes the range of these design parameters. The magnitudes of h_1 and h_2 are chosen to ensure that the average riblet height satisfies equation (1). Another key parameter is the unit denticle length, which governs the number of denticles along the streamwise direction. The front and rear side lengths, l_1 and l_2 , are expressed as ratios of the unit denticle length, rather than as absolute values. This method enhances flexibility in parameter selection and maintains alignment with the riblet design framework.

Table 1. Parametric setup for 3D riblet geometry.

3D riblet geometry parameters			
Parameter name	Symbol notation	Range	Unit
Primary ridge height	h_1	[0.08, 0.15]	mm
Side ridge height	h_2	[0.05, 0.10]	mm
Unit denticle length	L	[0.5, 1.5]	mm
Front side length ratio	l_1/L	[0.1, 0.4]	—
Rear side length ratio	l_2/L	[0.6, 0.9]	—

2.2. CFD setup

Figure 1(d) shows the current fluid domain configuration in ANSYS Fluent, featuring a quarter-cylindrical fluid region encompassing the towed array. A right-handed Cartesian coordinate system is introduced, with the z -axis aligned along the longitudinal direction (i.e. the freestream flow direction). Several boundary conditions are imposed, including a velocity inlet, a pressure outlet, and two symmetry planes. The exterior cylindrical boundary adjoining the symmetry planes is treated as a pressure outlet allowing for backflow. The array surface is modeled as a no-slip wall. A position-dependent meshing strategy is employed to allocate finer mesh near the array surface, incorporating 10 inflation layers in the near-wall region. The first layer thickness is set to $y^+ = 0.9$ and increases at a rate of 1.2. The mesh resolution over the riblet surface is set between $30 \mu\text{m}$ and $40 \mu\text{m}$ to accurately capture the topography and fluid dynamics within the boundary layer.

A wall-adapting local eddy-viscosity (WALE) sub-grid model is applied throughout both stages to close the momentum equations. The eddy viscosity is evaluated with the constant $c_w = 0.325$. On the present mesh this choice keeps the SGS-to-resolved dissipation ratio between 0.12 and 0.28 across the boundary layer, indicating adequate scale separation. The algebraic form of the WALE closure and its derivation are documented in supporting information S.1. Because the riblet surface is fully 3D, resolving the narrow grooves and sharp ridge tips forces the near-wall grid spacing into the micrometer range, a single wall-resolved large eddy simulation (LES) therefore requires high computational cost. Recent high-order implicit-LES (iLES) studies have shown that carefully designed weighted essentially non-oscillatory schemes can achieve direct numerical simulation (DNS) level fidelity in compressible TBLs without any explicit SGS term. Ritos *et al* demonstrated that ninth- to eleventh-order iLES accurately captures near-wall anisotropy and Reynolds stresses on meshes

significantly coarser than DNS [34, 35], while retaining excellent parallel efficiency. In future work we therefore plan to assess whether a high-order iLES formulation can further reduce the numerical cost of riblet optimization without compromising the acoustic and hydrodynamic accuracy.

In the previous work [18], simulation results indicate that adjusting riblet size can significantly lower hydrodynamic drag, suggesting that a smaller riblet size could be beneficial for both noise and drag reduction. However, the complex surface topography of 3D riblets presents a challenge, as reducing the riblet size dramatically increases the computational cost, with the meshing process alone taking several days. To address this, we propose a domain modification that scales the model size proportionally to the riblet size while maintaining a manageable number of surface cells. Specifically, we reduce the original domain size from 1000 mm to 100 mm, along with the corresponding array radius from 20 mm to 2 mm. The initial guess for dimensionless wavelength and amplitude, $s^+ = 25.2$ and $h^+ = 12.6$, are maintained, with the flow speed adjusted accordingly. Leveraging equations (1) and (2), the recommended flow speed is approximately 1 m s^{-1} (2 knots) based on the adjusted domain size.

The simulation is conducted in two stages. The first stage involves a preparatory run using LES and the energy equation to establish a quasi-developed state before initiating the acoustic analysis. This stage lasts for five flow passing times. In the second stage, the Ffowcs Williams–Hawkings (FWH) acoustic solver is applied concurrently with the LES solver for another 1000 time steps, with a time step size of 0.0004 s. Based on the Nyquist sampling theorem, the sound pressure level (SPL) spectra are captured up to 1250 Hz, with a maximum bin width of 2.5 Hz. The details of FWH formulation are documented in the supporting information S.2.

2.3. Bayesian optimization explorer

One of the primary targets of this study is to examine the potential of 3D riblets in mitigating flow-induced noise across different frequency bands. Since different topography designs exhibit varying performance across frequencies, efficiently identifying configurations that minimize noise within the targeted frequency range is essential. To this end, Bayesian optimization has been utilized for design exploration, leveraging its effectiveness in solving intricate black-box optimization problems, particularly when working with limited control variables and datasets [36]. This exploration framework seeks to identify a parameter set by addressing the following problem:

$$x_{\text{opt}} = \operatorname{argmin}_{x \in \chi} f(x) \quad (3)$$

where $x = (h_1, h_2, s, \frac{l_1}{L}, \frac{l_2}{L}, L)$ is the design parameter array, and χ represents the design space constrained by the thresholds specified in table 1. In this

study we treat hydrodynamic drag and flow-induced noise as two independent objectives in a bi-objective Bayesian-optimization framework. Rather than collapsing them into a single merit, the search is driven by the Pareto lower-confidence-bound acquisition rule. Specifically, the acoustic objective y_1 is based on the integrated sound power within strategically selected frequency windows that bracket the first and second dominant tonal peaks. The integrated sound power within a specified frequency range is numerically calculated as:

$$y_1 = P_{\text{target}} = \sum_i \frac{\text{PSD}(f_i) + \text{PSD}(f_{i+1})}{2} \cdot (f_{i+1} - f_i) \quad (4)$$

where $\text{PSD}(f_i)$ is the power spectral density (PSD) in $\mu\text{Pa}^2\text{Hz}^{-1}$ at frequency band f_i , and i are chosen to encapsulate the first and second peak sound signals, as further detailed in section 3.2. The drag-related objective y_2 , is the wall-shear stress on the array surface (Pa). Both objectives are evaluated sequentially via CFD simulations. After n simulations the data set is $\mathcal{D}_n = \{(x_i, y_{1,i}, y_{2,i})\}_{i=1}^n$. Each objective is modeled as an unknown deterministic function $f_j(\cdot)$ such that $y_{j,i} = f_j(x_i) + \varepsilon_{j,i}$, where $\varepsilon_{j,i} \sim \mathcal{N}(0, \sigma_j^2)$ is the Gaussian noise. At iteration n the Gaussian-process posteriors $f_j(x) | \mathcal{D}_n \sim \mathcal{N}(\mu_{j,n}(x), \sigma_{j,n}(x)^2)$ provide the mean-standard-deviation pairs $[\mu_{j,n}(x), \sigma_{j,n}(x)]$ for each objective, from which the vector of LCB $L_n(x)$ is constructed:

$$L_n(x) = \begin{bmatrix} \mu_{1,n}(x) - \kappa_n \sigma_{1,n}(x) \\ \mu_{2,n}(x) - \kappa_n \sigma_{2,n}(x) \end{bmatrix}. \quad (5)$$

The set of candidate points whose L_n vectors are non-dominated constitutes the optimistic Pareto set

$$\mathcal{S}_n = \{x \in \mathcal{X} : \nexists x^* \in \mathcal{X} \text{ s.t. } L_n(x^*) < L_n(x)\}. \quad (6)$$

To select a single design for evaluation we apply a deterministic linear scalarization with fixed weights $[w_1, w_2] = [0.8, 0.2]$. The next favorable design points is then determined through:

$$x_{n+1} = \arg \min_{x \in \mathcal{S}_n} [w_1 L_{1,n}(x) + w_2 L_{2,n}(x)]. \quad (7)$$

Because the application targets a TAS system, noise suppression is given priority in the optimization. The fixed weights therefore steer the deterministic linear scalarization toward the noise-optimal portion of the Pareto front, while the 20% drag weight still guards against designs with prohibitive shear stress. This accelerates convergence on low-noise designs, but may leave low-drag regions of the frontier less densely sampled. If design targets place higher priority on drag reduction, the weight vector can be re-assigned accordingly.

It is of note that κ is a tunable factor to balance exploitation and exploration. At the initial stage of optimization, we introduced random perturbations to each parameter by sampling from a uniform distribution, thereby generating 30 designs to serve as the initial pool for Bayesian optimization. A high exploration factor of $\kappa = 100$ was chosen to encourage exploration. Subsequently, κ was progressively reduced every 10 iterations to gradually shift the optimization strategy from exploration to exploitation [37, 38], facilitating the discovery of a near-optimal solution. Specifically, κ followed the decay sequence [100, 50, 10, 5, < 5], corresponding to the design point subsets $dp = [31 : 40, 41 : 50, 51 : 60, 61 : 70, 71 : 85]$.

3. Results

This section benchmarks the performance of a 3D RRAS design against a conventional smooth surface, focusing on variations in flow-induced noise and hydrodynamic drag. The analysis draws on CFD simulations of 85 designs—30 randomly generated and 55 optimized through Bayesian methods. The study provides insight into how riblet configurations influence performance, emphasizing the potential of riblet reinforcement to reduce flow noise and drag in TAS applications.

3.1. Overall sound pressure level (OASPL) and drag performance comparison

The analysis focuses initially on the OASPL, which quantifies the total acoustic power generated by the interaction between the array surface and seawater during towing operations (see equation (8)). In contrast to hydrodynamic drag, which reflects time-averaged resistance, acoustic emissions arise from unsteady pressure fluctuations across a range of frequencies. By jointly analyzing OASPL and wall shear stress, we observe that riblet configurations optimized through Bayesian multi-objective methods yield a spectrum of performance outcomes: some designs are particularly effective at suppressing flow noise, others at minimizing drag. A subset of configurations succeeds in achieving both objectives concurrently, demonstrating that sharkskin-inspired surface structures can enhance noise mitigation and hydrodynamic efficiency when carefully tuned. These improvements stem from the riblets' ability to reorganize near-wall turbulence, which in turn reduces both momentum loss and pressure fluctuation intensity, as further detailed in section 4,

$$\text{OASPL} = 10 \cdot \log_{10} \left(\sum_{(i=1)}^n 10^{0.1\text{SPL}(f_i)} \right). \quad (8)$$

To evaluate how riblets affect acoustic energy across the tested frequency range, we compared the OASPL and drag (represented by wall shear stress) of

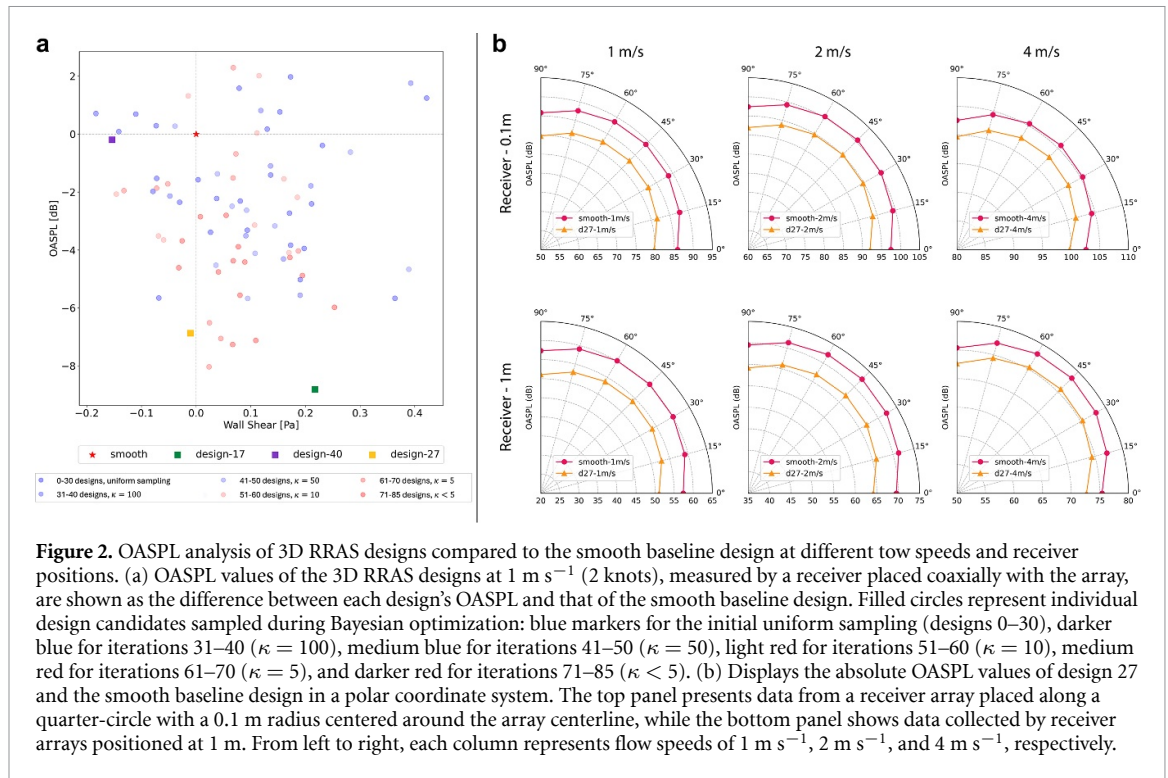


Figure 2. OASPL analysis of 3D RRAS designs compared to the smooth baseline design at different tow speeds and receiver positions. (a) OASPL values of the 3D RRAS designs at 1 m s^{-1} (2 knots), measured by a receiver placed coaxially with the array, are shown as the difference between each design's OASPL and that of the smooth baseline design. Filled circles represent individual design candidates sampled during Bayesian optimization: blue markers for the initial uniform sampling (designs 0–30), darker blue for iterations 31–40 ($\kappa = 100$), medium blue for iterations 41–50 ($\kappa = 50$), light red for iterations 51–60 ($\kappa = 10$), medium red for iterations 61–70 ($\kappa = 5$), and darker red for iterations 71–85 ($\kappa < 5$). (b) Displays the absolute OASPL values of design 27 and the smooth baseline design in a polar coordinate system. The top panel presents data from a receiver array placed along a quarter-circle with a 0.1 m radius centered around the array centerline, while the bottom panel shows data collected by receiver arrays positioned at 1 m. From left to right, each column represents flow speeds of 1 m s^{-1} , 2 m s^{-1} , and 4 m s^{-1} , respectively.

each RRAS design with those of a smooth baseline. We quantified the differences in OASPL and drag by subtracting the baseline values from those of each RRAS design. Figure 2(a) presents these differences, measured at a receiver located on the towed array's centerline $[0, 0, 0.05] \text{ m}$ at a towing speed of 1 m s^{-1} . The drag variation is shown on the x -axis, while the OASPL variation is shown on the y -axis. Color coded square markers highlight the designs that show the most significant performance gains. The design with the globally lowest flow noise is indicated by a green square marker. Notably, designs that reduce both flow noise and drag offer dual benefits for TAS applications. These designs reside in the 'desired quadrant' (the third quadrant of the coordinate system). Within this region, the designs achieving the lowest noise level and the lowest drag are identified by yellow and purple square markers, respectively.

To explore noise reduction at different towing speeds and receiver positions, we focus on Design 27, which is the quietest design in the desired quadrant of figure 2(a). We conduct additional simulations at 1 m s^{-1} , 2 m s^{-1} (~ 4 knots), and 4 m s^{-1} (~ 8 knots), as indicated in figure 2(b). Receivers are placed at radii of 0.1 m and 1 m, covering angles from 0° to 90° in 15° increments, to examine how noise reduction varies with distance and angle. These results shed light on near-field performance, which is crucial for maintaining a favorable signal to noise ratio, as well as far-field considerations relevant to marine life.

3.2. PSD analysis

The PSD characterizes the distribution of signal power across various frequency components, providing detailed insight into dominant energy levels within a signal. In practical applications, dominant noise sources appear as distinct peaks in the PSD, making them readily detectable by sonar systems or perceptible to marine organisms. Consequently, reducing flow-induced noise within these critical frequency bands is essential for enhancing the stealth capabilities of a TAS system. Figure 3(a) overlays the PSD of all 85 designs, illustrating the distribution of sound power across frequencies.

Two prominent peaks are observed in these spectra: the first near 250 Hz and the second around 750 Hz. These peaks consistently appear in both the smooth baseline and riblet-reinforced surface cases, indicating that they are characteristic of the inherent flow–structure interaction rather than artifacts introduced by the riblet geometry. It is hypothesized that the 250 Hz peak originates from large-scale vortex shedding and pressure oscillations around the cylindrical array body, with the 750 Hz peak representing a higher-order harmonic. The selected frequency range (0–1 kHz) encompasses the dominant flow-induced noise components typically observed in TAS systems and is therefore considered representative for evaluating acoustic performance. Although sound absorption in water increases with frequency, the attenuation below 1 kHz remains relatively modest.

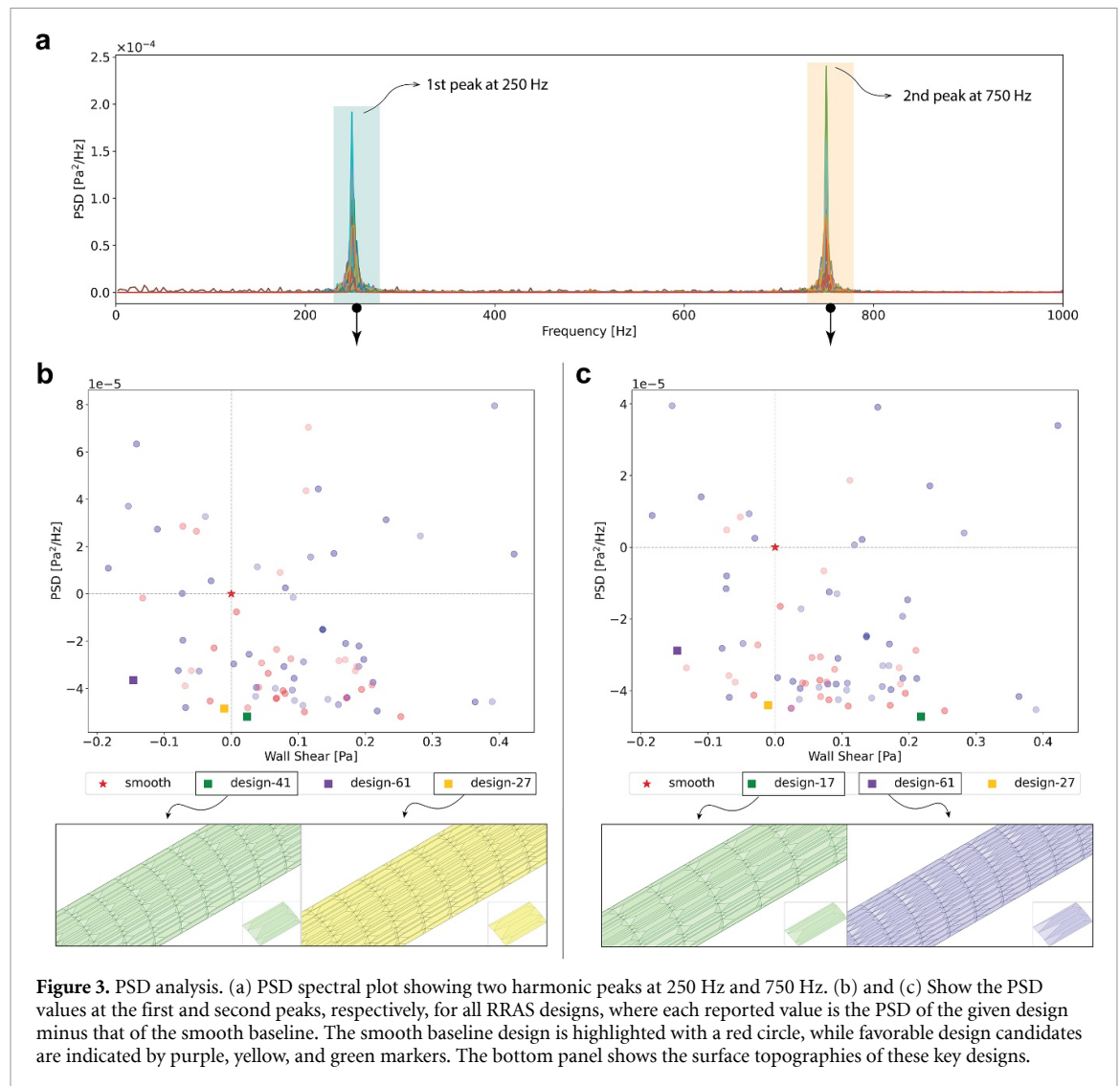


Figure 3. PSD analysis. (a) PSD spectral plot showing two harmonic peaks at 250 Hz and 750 Hz. (b) and (c) Show the PSD values at the first and second peaks, respectively, for all RRAS designs, where each reported value is the PSD of the given design minus that of the smooth baseline. The smooth baseline design is highlighted with a red circle, while favorable design candidates are indicated by purple, yellow, and green markers. The bottom panel shows the surface topographies of these key designs.

Based on the Thorp formula [39], the absorption coefficient at 250 Hz is approximately 0.04 dB km^{-1} , rising to only around 0.5 dB km^{-1} at 1 kHz, which is negligible over typical operational distances of tens to hundreds of meters. As such, the propagation loss due to absorption does not significantly reduce the relevance of noise within this frequency range, and it remains appropriate to target this band in the optimization process.

After identifying the dominant noise signals in the spectrum, we construct a performance space based on the magnitudes of the first and second PSD peaks. The peak PSD values for the riblet designs are benchmarked against those of the smooth baseline and plotted within the same coordinate system described in section 3.1, as shown in figures 3(b) and (c). Additionally, the surface topographies of the designs with the most significant performance improvements are highlighted in the figure. The corresponding metric statistics for these designs are summarized in table 2.

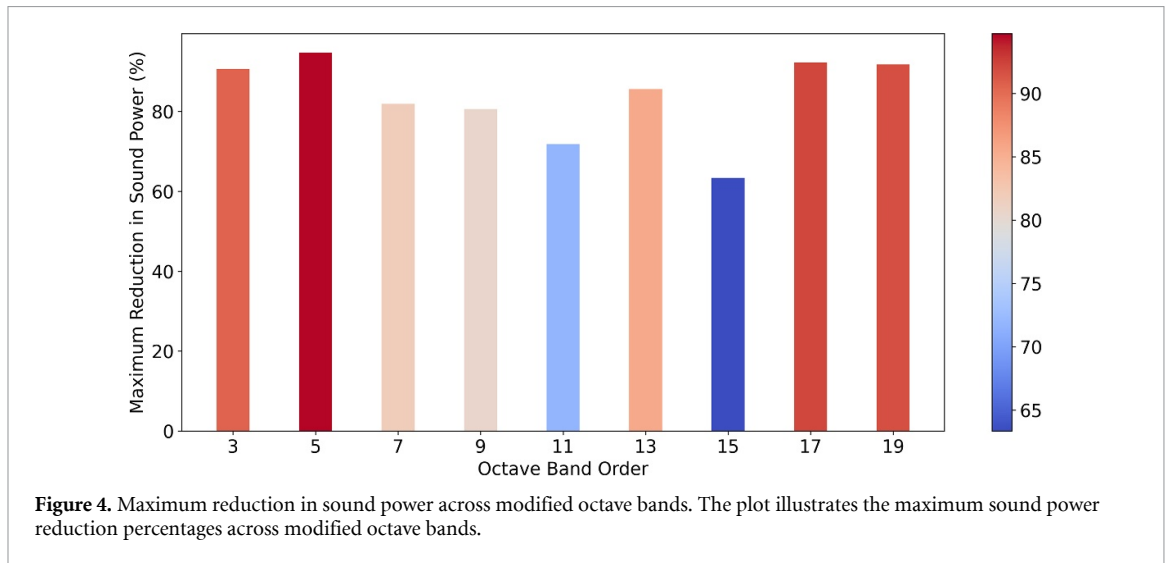
3.3. Frequency sensitivity evaluation using octave bands

Simulation results indicate that the RRAS's noise suppression is not uniformly effective across all frequencies; performance differences are observed, particularly in certain targeted bands. Therefore, this study further focuses on examining how noise suppression levels change in response to different frequencies. Understanding these variations is critical, as it enables the targeted optimization of RRAS towards strategic frequency ranges.

To conduct a detailed sensitivity analysis, we apply the widely recognized acoustic standard of one-third octave bands, which partition the sound spectrum into manageable sections. The mapping between the one-third octave band numbers and their corresponding frequency ranges is provided in the supporting information (see table S1). In this study, only the odd-numbered bands are retained, with their bandwidths extended by merging with adjacent even-numbered bands. The resulting modified

Table 2. Drag and PSD data benchmarked against smooth baseline.

Design ID	Wall shear (Pa)	PSD ($\text{Pa}^2 \text{Hz}^{-1}$)	Wall shear (%)	PSD (%)
Peak PSD against smooth baseline at 250 Hz				
41	0.024	-5.19×10^{-05}	+0.80	-95.30
61	-0.146	-3.65×10^{-05}	-4.91	-67.02
27	-0.010	-4.85×10^{-05}	-0.35	-89.08
Peak PSD against smooth baseline at 750 Hz				
17	0.218	-4.73×10^{-05}	+7.32	-96.91
61	-0.146	-2.89×10^{-05}	-4.91	-59.19
27	-0.01	-4.41×10^{-05}	-0.35	-90.33



octave bands, shown in table S2, offer enhanced segmentation for the analysis. Following this segmentation, the integrated sound power within each frequency range is calculated to assess the level of flow noise suppression. This integration is approximated by equation (4). The performance space corresponding to PSD benchmarking across different octave bands is presented in figure S1. The maximum sound power reduction within each frequency range was collected and plotted in figure 4.

3.4. Flow field analyses

To investigate the underlying fluid mechanics, we performed post-processing of CFD simulations. Our analysis focuses on how riblet structures influence surface vorticity, a key factor in flow-induced noise. Surface pressure fluctuations, driven by cyclical loading in the mean flow and random turbulent motions, are closely linked to noise levels. By altering vorticity dynamics in the near-wall region, riblets can mitigate these fluctuations, thereby reducing noise.

In particular, snapshots of the flow field properties at the end of the simulation ($t = 0.9s$) are extracted, as shown in figure 5. To visualize the dominant surface vortex structures, the iso-surfaces

of swirling strength for design 27 and the smooth baseline design are plotted at thresholds of 100 s^{-1} and 20 s^{-1} , respectively, as shown in figure 5(a). Moreover, figure 5(b) presents swirling strength contours of the flow at various cross sections. Each cross section captures a distinct phase of the flow as it moves through different segments of a single riblet unit. These contours elucidate the vorticity distribution over the RRAS and its deviation from that of a smooth surface. This difference highlights how fluctuations in wall pressure correspondingly influence flow noise generation. Lastly, figure 5(c) presents the second norm of the streamwise velocity gradient tensor (i.e. $\|\nabla w\|_2$), revealing the flow-wall interaction pattern and offering insight into why RRAS effectively reduces hydrodynamic drag.

While these snippets provide a detailed view of the flow patterns, they do not capture the transient interaction between the flow and the array surface, nor the resultant effects on flow noise and drag. For a more detailed analysis over time, Videos S1 and S2 show the iso-surfaces of the normalized Q -invariant at a value of 500, with color mapping based on local flow vorticity.

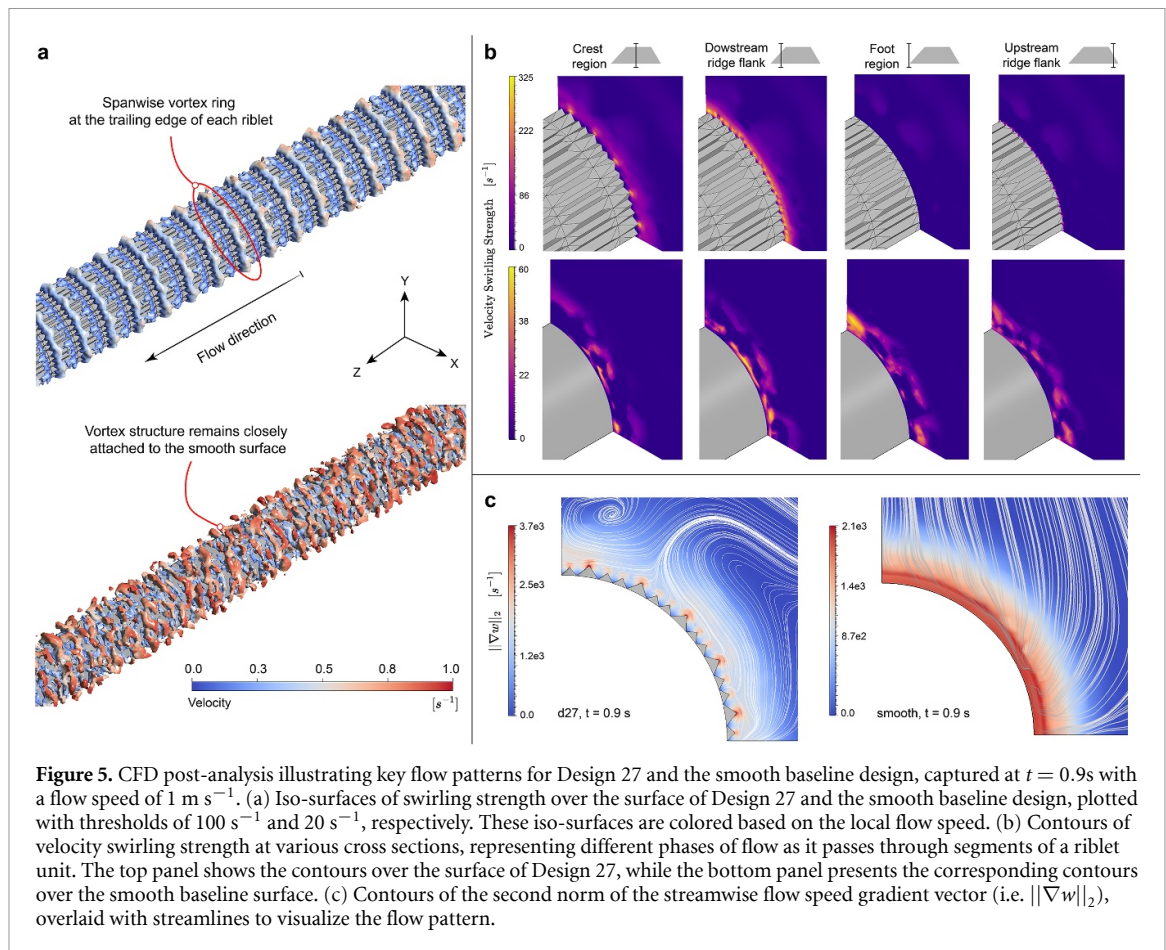


Figure 5. CFD post-analysis illustrating key flow patterns for Design 27 and the smooth baseline design, captured at $t = 0.9$ s with a flow speed of 1 m s^{-1} . (a) Iso-surfaces of swirling strength over the surface of Design 27 and the smooth baseline design, plotted with thresholds of 100 s^{-1} and 20 s^{-1} , respectively. These iso-surfaces are colored based on the local flow speed. (b) Contours of velocity swirling strength at various cross sections, representing different phases of flow as it passes through segments of a riblet unit. The top panel shows the contours over the surface of Design 27, while the bottom panel presents the corresponding contours over the smooth baseline surface. (c) Contours of the second norm of the streamwise flow speed gradient vector (i.e. $\|\nabla w\|_2$), overlaid with streamlines to visualize the flow pattern.

4. Discussion

As illustrated in figure 2(a), the RRAS designs demonstrate clear effectiveness in reducing hydrodynamic drag, consistent with the well-established drag-reducing capabilities of 2D denticle structures reported in prior studies. Despite the increased geometric complexity introduced by 3D configurations, our results show that several RRAS designs achieve substantial drag reduction. Design 40 exhibits the most significant improvement, with a 5.18% decrease in drag relative to the smooth baseline, highlighting the potential of carefully tuned riblet topographies to enhance flow efficiency. These results reaffirm the robustness of riblet-based drag reduction mechanisms and extend their applicability to complex, bioinspired surfaces optimized for underwater environments.

In addition to their impact on drag, many RRAS configurations also exhibit strong noise suppression capabilities. Most designs yield reductions in flow-induced noise, as indicated by their positions in the third and fourth quadrants of the performance space. Design 17, for instance, achieves the most substantial noise reduction, lowering the OASPL by 8.81 dB. Notably, the Bayesian multi-objective optimization process reveals designs that offer dual

benefits in both drag and noise reduction. Among them, Design 27 stands out by achieving a 6.87 dB reduction in OASPL while also decreasing drag, making it one of the most balanced and effective performers.

Furthermore, figure 2(b) shows that the 3D RRAS design consistently reduces flow noise at both the 0.1 m and 1 m circumferential receivers across various flow speeds. The polar plots indicate that the noise reduction is largely insensitive to the observation angle, with its overall magnitude remaining unaffected by changes in angle. However, the magnitude of reduction decreases as flow speed increases. For instance, at flow speeds of 1 m s^{-1} and 2 m s^{-1} , the average reduction is approximately 5–6 dB across different angles, whereas at 4 m s^{-1} it declines to 3–4 dB. This effect is anticipated, as the recommended riblet dimensions are inversely proportional to shear velocity, as indicated by equations (1) and (2). Accordingly, a reduction in riblet size may theoretically contribute to lower noise levels with increasing towing speed.

Design candidates identified through PSD analysis exhibit distinct performance advantages over those highlighted in the OASPL comparison, as illustrated in figure 3. Specifically, design 41 achieves a substantial reduction of 95.3% in the first PSD

peak, effectively minimizing dominant noise within the lower frequency range. Conversely, design 17 targets higher frequency noise, reaching a peak reduction of 96.9% in the second PSD peak. Design 61, on the other hand, demonstrates the most balanced overall performance by achieving a 4.91% decrease in hydrodynamic drag while simultaneously reducing the first and second PSD peaks by 67.0% and 59.2%, respectively. This combination of drag reduction and noise attenuation highlights Design 61 as an optimal trade-off between hydrodynamic efficiency and noise control, making it particularly suitable for applications where for instance both performance and stealth are essential. Based on the geometries shown in figures 3(b) and (c), it is hypothesized that a longer unit length (L), lower l_1 and l_2 ratios, and a higher main ridge height (h_1) contribute to enhanced flow noise suppression. Conversely, a higher l_1 ratio, combined with equal h_1 and h_2 , is associated with improved drag reduction.

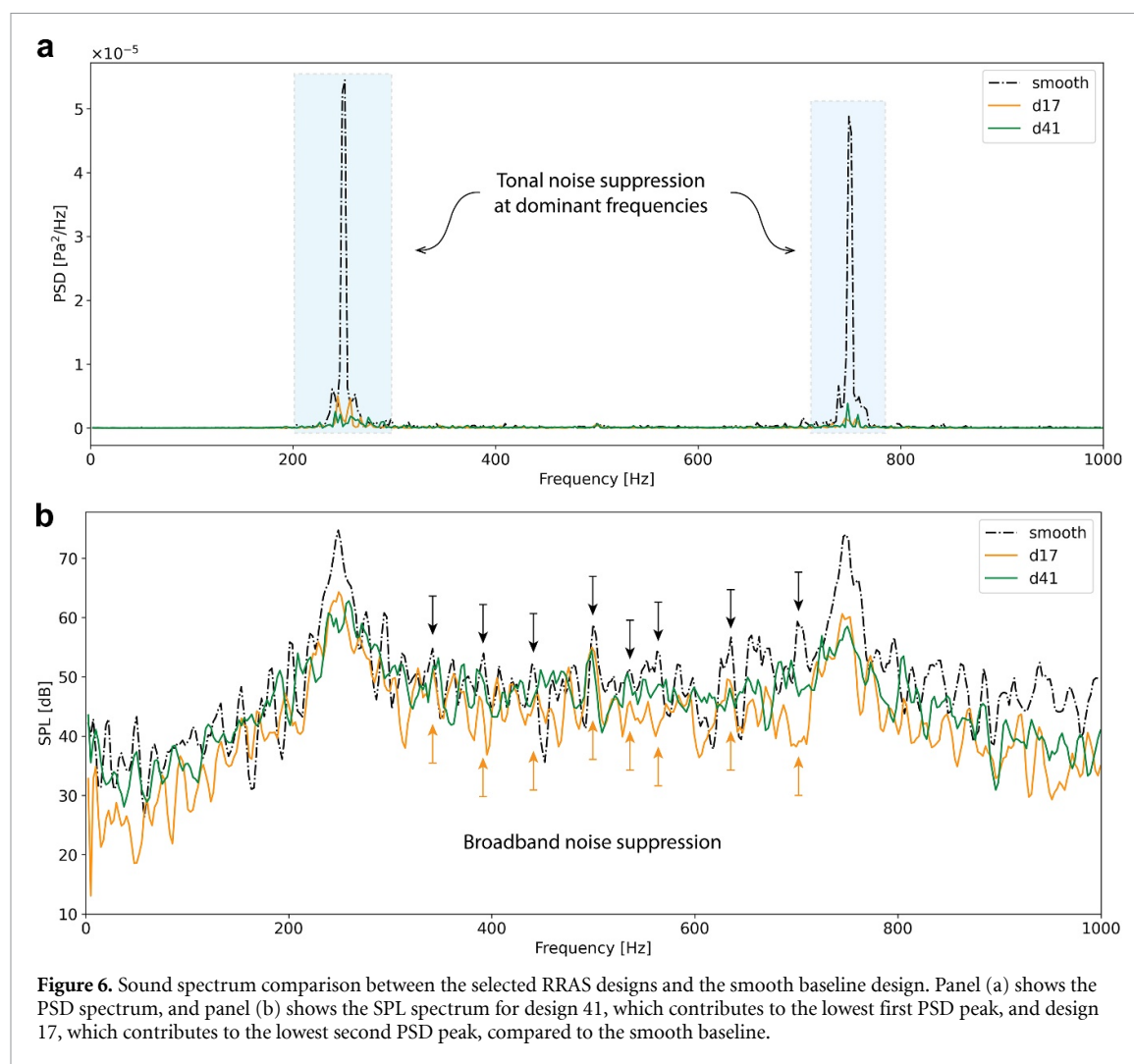
The color distribution in figures 2(a), 3(b) and (c) traces the optimization path from broad exploration to focused exploitation. Uniformly sampled designs (blue) scatter across all quadrants, seeding the Gaussian-process surrogates. As the exploration factor κ is stepped down (from light-blue to dark-red) the cloud drifts decisively below the horizontal baseline, confirming that nearly every subsequent design reduces peak-band PSD. Because the tie-breaker weights noise four times more than drag, later iterations tolerate moderate wall-shear increases when they secure larger acoustic gains; this prioritization is evidenced by red points in the lower-right quadrant. Nevertheless, many dark-red points settle in the desired quadrant, demonstrating that the algorithm also uncovers designs offering simultaneous noise and drag improvements. By maintaining and iteratively refining an explicit Pareto set, the multi-objective framework delivers a well-populated spectrum of optimal trade-offs that would be inaccessible to single-objective or sequential tuning approaches.

For a detailed comparison of the top-performing designs in flow noise reduction, figure 6 presents the noise suppression performance of Designs 17 and 41 relative to a smooth surface, using both PSD and SPL spectra. Notably, the SPL spectrum shown in the figure was first smoothed with a 9th-order Savitzky-Golay filter to remove noise and enhance the clarity of the overall trend. The spectra indicate that the dominant acoustic modes remain unchanged following the implementation of the RRAS, with the first and second peaks consistently occurring at 250 Hz and 750 Hz, respectively. These peaks correspond to the characteristic frequencies of flow turbulence, which dominate the spectral energy distribution. As shown in figure 6(a), the RRAS significantly reduces the amplitude of these peaks compared to the smooth

surface. A similar trend is observed in the SPL spectrum (figure 6(b)), where both RRAS designs exhibit lower peak noise levels. Moreover, the SPL spectra demonstrate that the noise reduction extends beyond tonal components at harmonic frequencies to include broadband suppression. Design 17 is particularly effective at reducing broadband noise, while Design 41 achieves greater attenuation of tonal peaks. The ability of the RRAS to suppress flow noise may result from the combined influence of vortex lifting and vortex ring ejection. As discussed later, these mechanisms help displace regions of intense pressure fluctuations caused by turbulence away from the array wall, thereby weakening the near-wall pressure sources and reducing the overall radiated noise.

The observed reduction in peak PSD potentially suggests an energy shift from lower to higher frequencies (i.e. $f > 1000$ Hz), a range not explored due to limitations in the current sampling rate. Based on these trends, it is likely that the third harmonic emerges above 2000 Hz. Investigating this higher frequency range would require halving the current time step size to maintain the same bin width, which is computationally prohibitive given available resources. Consequently, this limitation presents an opportunity for future research to explore effects in the higher frequency domain.

Building on the premise that 3D riblet topography effectively suppresses flow noise, this study aims to identify the frequency ranges where such suppression is most pronounced. As illustrated in figure 4, the 3D riblet designs achieve significant reductions in sound power within modified octave bands 3 and 5. However, these bands encompass narrow frequency ranges (see table S2), making the comparisons more susceptible to DC offset and other sources of bias. In contrast, the substantial reductions observed in bands 13 and 17 provide more reliable indicators of noise suppression efficacy. Bands 13 and 17 are pivotal to the noise profile of the TAS, with band 13 encompassing the first PSD peak at 250 Hz and band 17 capturing the second PSD peak at 750 Hz. It is of note that the integral of sound power within these two targeted frequency bands is defined as the objective function for Bayesian optimization. This approach leads to Design 32 achieving the maximum noise reduction in Band 13 (222.7–353.6 Hz), with an 85.6% decrease in total sound power within this band. Similarly, Design 17 attains the highest noise reduction in Band 17 (561.2–890.9 Hz), realizing a 92.2% reduction in sound power for that frequency range. When evaluating trade-offs, the data indicate that a favorable balance between drag reduction and flow noise minimization is attainable. For instance, within Band 13, Design 27 achieves a 35.2% reduction in sound power alongside a 4.9% decrease in drag. Similarly, in Band 17, Design 40 results in a 14.7% reduction in sound power and a 5.18% decrease in drag. These findings



highlight the potential to optimize riblet designs to enhance acoustic performance within strategic frequency ranges and improve hydrodynamic efficiency in RRAS applications.

CFD post-analysis provides comprehensive insights into the mechanisms underlying the RRAS's improved noise suppression and drag reduction performance. As illustrated in figure 5(a), the RRAS induces distinct surface flow patterns characterized by the formation of vortex ring structures at the rear of each riblet unit. These vortex rings detach from the riblets, thereby reducing the wetted area exposed to turbulent flow. In contrast, the smooth baseline design allows small eddies to remain closely attached to the surface, resulting in higher-intensity pressure fluctuations, as evidenced by the PSD analysis. Figure 5(b) further supports this observation. The swirling-strength contours reveal that rapid rotation occurs predominantly near each riblet's crest, thereby limiting the interaction area with the flow. This confinement effectively decreases the wetted area of the RRAS in regions of vortex flow, consequently reducing sound power intensity. Conversely, the strong swirling regions in the smooth baseline design remain

closely adhered to the surface, potentially contributing to intensified pressure fluctuations. Regarding drag reduction, figure 5(c) shows that the magnitude of streamwise velocity gradient is particularly high in the vicinity of the riblet crests and decreases in regions farther away within the TBL. In contrast, the smooth surface maintains a more uniformly high velocity gradient near the wall, leading to greater momentum loss during flow-wall interactions. These findings elucidate how the RRAS design optimizes acoustic performance by altering surface flow dynamics.

Beyond their role in noise suppression, denticle-inspired riblet structures reduce drag by fundamentally altering the momentum transfer mechanisms within the near-wall region. Specifically, the angled ridges and valleys characteristic of the 3D RRAS geometry guide high-momentum fluid along streamwise-aligned pathways, minimizing cross-stream momentum diffusion that typically drives turbulent energy production. This anisotropic surface guidance restricts the lateral oscillation and bursting of near-wall vortices, which are primary contributors to skin friction in TBLs. Moreover, the riblet-induced modulation of local shear layers effectively dampens

turbulent transport toward the wall, allowing for lower energy dissipation rates in the viscous sub-layer. These effects collectively delay the breakdown of streamwise coherence in the flow and result in a measurable reduction in wall shear stress, underpinning the drag reduction benefits observed in high-performing RRAS designs such as Design 40.

Notably, a quasi-static, snapshot-based analysis provides only limited insights into the underlying mechanisms. Although theoretically useful, it does not fully capture the flow's continuous time-dependent behavior. Videos S1 and S2 offer a clearer perspective on the fluid dynamics. In particular, the normalized Q -invariant iso-surfaces indicate that the streamwise trapezoidal pattern in the RRAS tends to segregate vortical structures, leading to the detachment effect shown in figure 5(a). By contrast, vortices on the smooth surface remains closely attached. Additionally, local vorticity renderings indicate that, on the smooth baseline surface, larger vortex structures can form and sustain higher rotational speeds. This phenomenon intensifies near-wall interactions and amplifies pressure fluctuations, thereby increasing flow noise. In contrast, the RRAS disrupts these coherent structures, reducing rotational speeds and diminishing pressure fluctuation levels, which ultimately lowers noise.

5. Conclusion

The findings presented in this study highlight the substantial potential of 3D riblet designs inspired by dermal denticles in enhancing the hydrodynamic and acoustic performance of TAS systems. Through extensive CFD simulations and Bayesian optimization, we demonstrated that the implementation of RRAS can achieve significant reductions in both drag and flow-induced noise. The results revealed that optimal 3D riblet configurations effectively suppress sound pressure levels across key frequency bands while maintaining or even improving hydrodynamic efficiency. This dual functionality underscores the advantages of bioinspired topographies in addressing critical performance challenges faced by underwater detection systems.

Our analysis further emphasizes the importance of parameterizing riblet geometries to achieve desired performance outcomes. Regarding OASPL, Design 17 achieves an 8.81 dB reduction but increases drag by 7.34%, whereas Design 27 lowers OASPL by 6.87 dB with a 0.34% drag reduction. Overall, Bayesian optimization successfully identified diverse RRAS designs that balance noise reduction and drag mitigation. Moreover, the 3D RRAS design consistently and omnidirectionally reduces flow noise across different flow speeds and receiving distances. In PSD analysis, Designs 41 and 17 showcase exceptional noise reduction, with up to 95.3% suppression at the first PSD peak (250 Hz) and 96.9% at

the second peak (750 Hz). Additionally, Design 61 provides a 67.0% reduction in the first PSD peak and 59.2% in the second while achieving a 4.91% drag reduction, positioning it as an optimal design for balancing both noise and drag performance. One of the original goals of this research was to assess whether the engineering problem presented a fruitful space for optimization. Rather than targeting a specific mission, we used a multi-objective algorithm to search for regions where flow noise could be suppressed while also improving drag performance for maritime operators. Since the aim was to identify solutions generalized across variables such as towing speed and towline diameter, discovering favorable microstructures for any frequency band in figure 4 is considered a key outcome and a strong foundation for future fixed-requirement missions.

Flow field analyses reveal that the 3D riblet designs generate distinct vortex ring structures that detach from the riblet surface, reducing the wetted area exposed to the TBL and contributing to lower drag and noise levels. In contrast, smooth baseline surfaces exhibit coherent vortices that remain attached, which intensify near-wall pressure fluctuations and increase flow noise. Furthermore, swirling-strength contours indicate that riblets confine regions of intense rotation near the riblet crests, minimizing their interaction with the surface and reducing the turbulent pressure fluctuations, which are primary contributors to acoustic emissions. Complementing these acoustic benefits, the riblet geometries also reduce hydrodynamic drag by modulating momentum transfer within the boundary layer, channeling flow along streamwise directions and suppressing lateral mixing. Together, these mechanisms highlight the dual functionality of 3D riblet designs in enhancing both acoustic properties and hydrodynamic efficiency.

The insights gained from this study pave the way for future investigations into scaling 3D riblet designs for full-scale towed arrays and exploring their applications across broader hydrodynamic contexts. Further refinement of riblet geometries and experimental validation could unlock new frontiers in bioinspired engineering, fostering innovations that extend beyond marine applications to aerospace and other fluid-dynamic systems.

Data availability statement

All data that support the findings of this study are included within the article (and any supplementary files).

Acknowledgment

We acknowledge support from MIT Lincoln Laboratory, CITRIS and the Banatao Institute,

National Science Foundation (Fund number: ACI-1548562), and Prytanean Foundation. DISTRIBUTION STATEMENT A. Approved for public release. Distribution is unlimited. This material is based upon work supported by the Department of the Air Force under Air Force Contract No. FA8702-15-D-0001. Any opinions, findings, conclusions or recommendations expressed in this material are those of the author(s) and do not necessarily reflect the views of the Department of the Air Force. © 2025 Massachusetts Institute of Technology. Delivered to the U.S. Government with Unlimited Rights, as defined in DFARS Part 252.227-7013 or 7014 (Feb 2014). Notwithstanding any copyright notice, U.S. Government rights in this work are defined by DFARS 252.227-7013 or DFARS 252.227-7014 as detailed above. Use of this work other than as specifically authorized by the U.S. Government may violate any copyrights that exist in this work.

Conflict of interest

The authors declare no competing interests.

ORCID iDs

Justin Rey  0009-0003-1564-8993

Matthew Jones  0009-0000-9788-0793

Grace X Gu  0000-0001-7118-3228

References

- Geyer T, Sarradj E and Fritzsche C 2009 Silent owl flight: experiments in the aeroacoustic wind tunnel NAG/DAGA pp 734–6
- Park K, Song C, Park J and Ryu S 2023 Multi-objective Bayesian optimization for the design of nacre-inspired composites: optimizing and understanding biomimetics through AI *Mater. Horiz.* **10** 4329–43
- Wei Z, Wang S, Farris S, Chennuri N, Wang N, Shinsato S, Demir K, Horii M and Gu G X 2024 Towards silent and efficient flight by combining bioinspired owl feather serrations with cicada wing geometry *Nat. Commun.* **15** 4337
- Vangelatos Z, Yildizdag M E and Grigoropoulos C P 2023 A designer's challenge: unraveling the architected structure of deep sea sponges for lattice mechanical metamaterials *Extreme Mech. Lett.* **61** 102013
- Egan P, Sinko R, LeDuc P R and Keten S 2015 The role of mechanics in biological and bio-inspired systems *Nat. Commun.* **6** 1–12
- Zamanian A H and Voltzow J 2024 Soft robots and soft bodies: biological insights into the structure and function of fluidic soft robots *Bioinspir. Biomim.* **20** 013001
- Lew A J, Stifler C A, Cantamessa A, Tits A, Ruffoni D, Gilbert P U P A and Buehler M J 2023 Deep learning virtual indenter maps nanoscale hardness rapidly and non-destructively, revealing mechanism and enhancing bioinspired design *Matter* **6** 1975–91
- Nepal D et al 2023 Hierarchically structured bioinspired nanocomposites *Nat. Mater.* **22** 18–35
- Cote B, Casey C and Jankauski M 2024 Wing inertia influences the phase and amplitude relationships between thorax deformation and flapping angle in bumblebees *Bioinspir. Biomim.* **20** 014001
- Lim D D, Ibarra A, Lee J, Jung J, Choi W and Gu G X 2025 A tunable metamaterial microwave absorber inspired by chameleon's color-changing mechanism *Sci. Adv.* **11** eads3499
- Dean B and Bhushan B 2010 Shark-skin surfaces for fluid-drag reduction in turbulent flow: a review *Phil. Trans. R. Soc. A* **368** 4775–806
- Bhushan B 2024 *Introduction to Biomimetics and Bioinspiration: Materials and Surfaces for Green Science and Technology* (Springer) pp 469–542
- Bandyopadhyay P R and Hellum A M 2014 Modeling how shark and dolphin skin patterns control transitional wall-turbulence vorticity patterns using spatiotemporal phase reset mechanisms *Sci. Rep.* **4** 6650
- Ott J, Lazalde M and Gu G X 2020 Algorithmic-driven design of shark denticle bioinspired structures for superior aerodynamic properties *Bioinspir. Biomim.* **15** 026001
- Frohnepfel B, Jovanović J and Delgado A 2007 Experimental investigations of turbulent drag reduction by surface-embedded grooves *J. Fluid Mech.* **590** 107–16
- Wang Y, Huang Y and Fu S 2022 On the tip sharpness of riblets for turbulent drag reduction *Acta Mech. Sin.* **38** 321389
- El-Samni O, Chun H and Yoon H 2007 Drag reduction of turbulent flow over thin rectangular riblets *Int. J. Eng. Sci.* **45** 436–54
- Wei Z, Zhang Z, Lim D D, Rey J, Jones M and Gu G X 2024 Influence of bioinspired riblet topographies on the mitigation of flow-induced noise in towed sonar arrays *Extrem. Mech. Lett.* **67** 102130
- Lasky M, Doolittle R D, Simmons B and Lemon S 2004 Recent progress in towed hydrophone array research *IEEE J. Ocean. Eng.* **29** 374–87
- Beerens S, Van Ijsselmuide S, Volwerk C, Trouvé E and Doisy Y 1999 *Flow Noise Analysis of Towed Sonar Arrays* (Nexus Media Limited)
- Unnikrishnan K, Pallayil V, Chitre M and Kuselan S *OCEANS 2011 IEEE-Spain* (IEEE) pp 1–4
- Capon J 1969 High-resolution frequency-wavenumber spectrum analysis *Proc. IEEE* **57** 1408–18
- Astley R, Macaulay G and Coyette J 1994 Mapped wave envelope elements for acoustical radiation and scattering *J. Sound Vib.* **170** 97–118
- Van Mierlo G, Beerens S, Been R, Doisy Y and Trouvé E 1997 Port-Starboard discrimination on hydrophone triplets in active and passive towed arrays *UDT97 vol 6* pp 113–6
- Knight A 1996 Flow noise calculations for extended hydrophones in fluid-and solid-filled towed arrays *J. Acoust. Soc. Am.* **100** 245–51
- Heidarian A, Ghassemi H and Liu P 2018 Numerical analysis of the effects of riblets on drag reduction of a flat plate *J. Appl. Fluid Mech.* **11** 679–88
- Ran W, Zare A and Jovanović M R 2021 Model-based design of riblets for turbulent drag reduction *J. Fluid Mech.* **906** A7
- Krieger V, Perić R, Jovanović J, Lienhart H and Delgado A 2018 Toward design of the antiturbulence surface exhibiting maximum drag reduction effect *J. Fluid Mech.* **850** 262–303
- Wen L, Weaver J C, Thornycroft P J M and Lauder G V 2015 Hydrodynamic function of biomimetic shark skin: effect of denticle pattern and spacing *Bioinspir. Biomim.* **10** 066010
- Oeffner J and Lauder G V 2012 The hydrodynamic function of shark skin and two biomimetic applications *J. Exp. Biol.* **215** 785–95
- Sayama S, Natsuhara M, Shinohara G, Maeda M and Tanaka H 2024 Three-dimensional shape of natural riblets in the white shark: relationship between the denticle morphology and swimming speed of sharks *J. R. Soc. Interface* **21** 20240063
- Lee S-J and Lee S-H 2001 Flow field analysis of a turbulent boundary layer over a riblet surface *Exp. Fluids* **30** 153–66
- Wen L, Weaver J C and Lauder G V 2014 Biomimetic shark skin: design, fabrication and hydrodynamic function *J. Exp. Biol.* **217** 1656–66

- [34] Ritos K, Kokkinakis I W and Drikakis D 2018 Physical insight into the accuracy of finely-resolved iLES in turbulent boundary layers *Comput. Fluids* **169** 309–16
- [35] Ritos K, Kokkinakis I W and Drikakis D 2018 Performance of high-order implicit large eddy simulations *Comput. Fluids* **173** 307–12
- [36] Shahriari B, Swersky K, Wang Z, Adams R P and De Freitas N 2015 Taking the human out of the loop: a review of Bayesian optimization *Proc. IEEE* **104** 148–75
- [37] Bian C, Wang X, Liu C, Xie X and Haitao L 2021 *IOP Conf. Ser.: Mater. Sci. Eng.* **1081** 012023
- [38] Dai Z, Yu H, Low B K H and Jaillet P *Int. Conf. on Machine Learning*. (PMLR) pp 1496–506
- [39] Fisher F and Simmons V 1977 Sound absorption in sea water *J. Acoust. Soc. Am.* **62** 558–64